

Measurement of the $D_s^+ \rightarrow \ell^+ \nu_\ell$ branching fractions and the decay constant $f_{D_s^+}$

M. Ablikim¹, M. N. Achasov^{9,e}, X. C. Ai¹, O. Albayrak⁵, M. Albrecht⁴, D. J. Ambrose⁴⁴, A. Amoroso^{49A,49C}, F. F. An¹, Q. An^{46,a}, J. Z. Bai¹, O. Bakina²³, R. Baldini Ferroli^{20A}, Y. Ban³¹, D. W. Bennett¹⁹, J. V. Bennett⁵, M. Bertani^{20A}, D. Bettoni^{21A}, J. M. Bian⁴³, F. Bianchi^{49A,49C}, E. Boger^{23,c}, I. Boyko²³, R. A. Briere⁵, H. Cai⁵¹, X. Cai^{1,a}, O. Cakir^{40A}, A. Calcaterra^{20A}, G. F. Cao¹, S. A. Cetin^{40B}, J. F. Chang^{1,a}, G. Chelkov^{23,c,d}, G. Chen¹, H. S. Chen¹, H. Y. Chen², J. C. Chen¹, M. L. Chen^{1,a}, S. Chen⁴¹, S. J. Chen²⁹, X. Chen^{1,a}, X. R. Chen²⁶, Y. B. Chen^{1,a}, H. P. Cheng¹⁷, X. K. Chu³¹, G. Cibinetto^{21A}, H. L. Dai^{1,a}, J. P. Dai³⁴, A. Dbeyssi¹⁴, D. Dedovich²³, Z. Y. Deng¹, A. Denig²², I. Denysenko²³, M. Destefanis^{49A,49C}, F. De Mori^{49A,49C}, Y. Ding²⁷, C. Dong³⁰, J. Dong^{1,a}, L. Y. Dong¹, M. Y. Dong^{1,a}, Z. L. Dou²⁹, S. X. Du⁵³, P. F. Duan¹, J. Z. Fan³⁹, J. Fang^{1,a}, S. S. Fang¹, X. Fang^{46,a}, Y. Fang¹, R. Farinelli^{21A,21B}, L. Fava^{49B,49C}, F. Feldbauer²², G. Felici^{20A}, C. Q. Feng^{46,a}, E. Fioravanti^{21A}, M. Fritsch^{14,22}, C. D. Fu¹, Q. Gao¹, X. L. Gao^{46,a}, X. Y. Gao², Y. Gao³⁹, Z. Gao^{46,a}, I. Garzia^{21A}, K. Goetzen¹⁰, L. Gong³⁰, W. X. Gong^{1,a}, W. Gradl²², M. Greco^{49A,49C}, M. H. Gu^{1,a}, Y. T. Gu¹², Y. H. Guan¹, A. Q. Guo¹, L. B. Guo²⁸, R. P. Guo¹, Y. Guo¹, Y. P. Guo²², Z. Haddadi²⁵, A. Hafner²², S. Han⁵¹, X. Q. Hao¹⁵, F. A. Harris⁴², K. L. He¹, T. Held⁴, Y. K. Heng^{1,a}, Z. L. Hou¹, C. Hu²⁸, H. M. Hu¹, J. F. Hu^{49A,49C}, T. Hu^{1,a}, Y. Hu¹, G. S. Huang^{46,a}, J. S. Huang¹⁵, X. T. Huang³³, X. Z. Huang²⁹, Y. Huang²⁹, Z. L. Huang²⁷, T. Hussain⁴⁸, W. Ikegami Andersson⁵⁰, Q. Ji¹, Q. P. Ji³⁰, X. B. Ji¹, X. L. Ji^{1,a}, L. W. Jiang⁵¹, X. S. Jiang^{1,a}, X. Y. Jiang³⁰, J. B. Jiao³³, Z. Jiao¹⁷, D. P. Jin^{1,a}, S. Jin¹, T. Johansson⁵⁰, A. Julin⁴³, N. Kalantar-Nayestanaki²⁵, X. L. Kang¹, X. S. Kang³⁰, M. Kavatsyuk²⁵, B. C. Ke⁵, P. Kiese²², R. Kliemt¹⁴, B. Kloss²², O. B. Kolcu^{40B,h}, B. Kopf⁴, M. Kornicer⁴², A. Kupsc⁵⁰, W. Kühn²⁴, J. S. Lange²⁴, M. Lara¹⁹, P. Larin¹⁴, C. Leng^{49C}, C. Li⁵⁰, Cheng Li^{46,a}, D. M. Li⁵³, F. Li^{1,a}, F. Y. Li³¹, G. Li¹, H. B. Li¹, H. J. Li¹, J. C. Li¹, Jin Li³², K. Li³³, K. Li¹³, Lei Li³, P. R. Li⁴¹, Q. Y. Li³³, T. Li³³, W. D. Li¹, W. G. Li¹, X. L. Li³³, X. N. Li^{1,a}, X. Q. Li³⁰, Y. B. Li², Z. B. Li³⁸, H. Liang^{46,a}, Y. F. Liang³⁶, Y. T. Liang²⁴, G. R. Liao¹¹, D. X. Lin¹⁴, B. Liu³⁴, B. J. Liu¹, C. X. Liu¹, D. Liu^{46,a}, F. H. Liu³⁵, Fang Liu¹, Feng Liu⁶, H. B. Liu¹², H. H. Liu¹, H. H. Liu¹⁶, H. M. Liu¹, J. Liu¹, J. B. Liu^{46,a}, J. P. Liu⁵¹, J. Y. Liu¹, K. Liu³⁹, K. Y. Liu²⁷, L. D. Liu³¹, P. L. Liu^{1,a}, Q. Liu⁴¹, S. B. Liu^{46,a}, X. Liu²⁶, Y. B. Liu³⁰, Z. A. Liu^{1,a}, Zhiqing Liu²², H. Loehner²⁵, X. C. Lou^{1,a,g}, H. J. Lu¹⁷, J. G. Lu^{1,a}, Y. Lu¹, Y. P. Lu^{1,a}, C. L. Luo²⁸, M. X. Luo⁵², T. Luo⁴², X. L. Luo^{1,a}, X. R. Lyu⁴¹, F. C. Ma²⁷, H. L. Ma¹, L. L. Ma³³, M. M. Ma¹, Q. M. Ma¹, T. Ma¹, X. N. Ma³⁰, X. Y. Ma^{1,a}, Y. M. Ma³³, F. E. Maas¹⁴, M. Maggiora^{49A,49C}, Y. J. Mao³¹, Z. P. Mao¹, S. Marcello^{49A,49C}, J. G. Messchendorp²⁵, J. Min^{1,a}, T. J. Min¹, R. E. Mitchell¹⁹, X. H. Mo^{1,a}, Y. J. Mo⁶, C. Morales Morales¹⁴, N. Yu. Muchnoi^{9,e}, H. Muramatsu⁴³, Y. Nefedov²³, F. Nerling¹⁴, I. B. Nikolaev^{9,e}, Z. Ning^{1,a}, S. Nisar⁸, S. L. Niu^{1,a}, X. Y. Niu¹, S. L. Olsen³², Q. Ouyang^{1,a}, S. Pacetti^{20B}, Y. Pan^{46,a}, P. Patteri^{20A}, M. Pelizaeus⁴, H. P. Peng^{46,a}, K. Peters^{10,i}, J. Pettersson⁵⁰, J. L. Ping²⁸, R. G. Ping¹, R. Poling⁴³, V. Prasad¹, H. R. Qi², M. Qi²⁹, S. Qian^{1,a}, C. F. Qiao⁴¹, L. Q. Qin³³, N. Qin⁵¹, X. S. Qin¹, Z. H. Qin^{1,a}, J. F. Qiu¹, K. H. Rashid⁴⁸, C. F. Redmer²², M. Ripka²², G. Rong¹, Ch. Rosner¹⁴, X. D. Ruan¹², A. Sarantsev^{23,f}, M. Savrié^{21B}, K. Schoenning⁵⁰, S. Schumann²², W. Shan³¹, M. Shao^{46,a}, C. P. Shen², P. X. Shen³⁰, X. Y. Shen¹, H. Y. Sheng¹, M. Shi¹, W. M. Song¹, X. Y. Song¹, S. Sosio^{49A,49C}, S. Spataro^{49A,49C}, G. X. Sun¹, J. F. Sun¹⁵, S. S. Sun¹, X. H. Sun¹, Y. J. Sun^{46,a}, Y. Z. Sun¹, Z. J. Sun^{1,a}, Z. T. Sun¹⁹, C. J. Tang³⁶, X. Tang¹, I. Tapan^{40C}, E. H. Thorndike⁴⁴, M. Tiemens²⁵, M. Ullrich²⁴, I. Uman^{40D}, G. S. Varner⁴², B. Wang³⁰, B. L. Wang⁴¹, D. Wang³¹, D. Y. Wang³¹, K. Wang^{1,a}, L. L. Wang¹, L. S. Wang¹, M. Wang³³, P. Wang¹, P. L. Wang¹, W. Wang^{1,a}, W. P. Wang^{46,a}, X. F. Wang³⁹, Y. Wang³⁷, Y. D. Wang¹⁴, Y. F. Wang^{1,a}, Y. Q. Wang²², Z. Wang^{1,a}, Z. G. Wang^{1,a}, Z. H. Wang^{46,a}, Z. Y. Wang¹, Z. Y. Wang¹, T. Weber²², D. H. Wei¹¹, P. Weidenkaff²², S. P. Wen¹, U. Wiedner⁴, M. Wolke⁵⁰, L. H. Wu¹, L. J. Wu¹, Z. Wu^{1,a}, L. Xia^{46,a}, L. G. Xia³⁹, Y. Xia¹⁸, D. Xiao¹, H. Xiao⁴⁷, Z. J. Xiao²⁸, Y. G. Xie^{1,a}, Q. L. Xiu^{1,a}, G. F. Xu¹, J. J. Xu¹, L. Xu¹, Q. J. Xu¹³, Q. N. Xu⁴¹, X. P. Xu³⁷, L. Yan^{49A,49C}, W. B. Yan^{46,a}, W. C. Yan^{46,a}, Y. H. Yan¹⁸, H. J. Yang^{34,j}, H. X. Yang¹, L. Yang⁵¹, Y. X. Yang¹¹, M. Ye^{1,a}, M. H. Ye⁷, J. H. Yin¹, B. X. Yu^{1,a}, C. X. Yu³⁰, J. S. Yu²⁶, C. Z. Yuan¹, W. L. Yuan²⁹, Y. Yuan¹, A. Yuncu^{40B,b}, A. A. Zafar⁴⁸, A. Zallo^{20A}, Y. Zeng¹⁸, Z. Zeng^{46,a}, B. X. Zhang¹, B. Y. Zhang^{1,a}, C. Zhang²⁹, C. C. Zhang¹, D. H. Zhang¹, H. H. Zhang³⁸, H. Y. Zhang^{1,a}, J. Zhang¹, J. J. Zhang¹, J. L. Zhang¹, J. Q. Zhang¹, J. W. Zhang^{1,a}, J. Y. Zhang¹, J. Z. Zhang¹, K. Zhang¹, L. Zhang¹, S. Q. Zhang³⁰, X. Y. Zhang³³, Y. Zhang¹, Y. H. Zhang^{1,a}, Y. N. Zhang⁴¹, Y. T. Zhang^{46,a}, Yu Zhang⁴¹, Z. H. Zhang⁶, Z. P. Zhang⁴⁶, Z. Y. Zhang⁵¹, G. Zhao¹, J. W. Zhao^{1,a}, J. Y. Zhao¹, J. Z. Zhao^{1,a}, Lei Zhao^{46,a}, Ling Zhao¹, M. G. Zhao³⁰, Q. Zhao¹, Q. W. Zhao¹, S. J. Zhao⁵³, T. C. Zhao¹, Y. B. Zhao^{1,a}, Z. G. Zhao^{46,a}, A. Zhemchugov^{23,c}, B. Zheng⁴⁷, J. P. Zheng^{1,a}, W. J. Zheng³³, Y. H. Zheng⁴¹, B. Zhong²⁸, L. Zhou^{1,a}, X. Zhou⁵¹, X. K. Zhou^{46,a}, X. R. Zhou^{46,a}, X. Y. Zhou¹, K. Zhu¹, K. J. Zhu^{1,a}, S. Zhu¹, S. H. Zhu⁴⁵, X. L. Zhu³⁹, Y. C. Zhu^{46,a}, Y. S. Zhu¹, Z. A. Zhu¹, J. Zhuang^{1,a}, L. Zotti^{49A,49C}, B. S. Zou¹, J. H. Zou¹

(BESIII Collaboration)

¹ Institute of High Energy Physics, Beijing 100049, People's Republic of China

² Beihang University, Beijing 100191, People's Republic of China

³ Beijing Institute of Petrochemical Technology, Beijing 102617, People's Republic of China

⁴ Bochum Ruhr-University, D-44780 Bochum, Germany

⁵ Carnegie Mellon University, Pittsburgh, Pennsylvania 15213, USA

⁶ Central China Normal University, Wuhan 430079, People's Republic of China

⁷ China Center of Advanced Science and Technology, Beijing 100190, People's Republic of China

⁸ COMSATS Institute of Information Technology, Lahore, Defence Road, Off Raiwind Road, 54000 Lahore, Pakistan

⁹ G.I. Budker Institute of Nuclear Physics SB RAS (BINP), Novosibirsk 630090, Russia

¹⁰ GSI Helmholtzcentre for Heavy Ion Research GmbH, D-64291 Darmstadt, Germany

¹¹ Guangxi Normal University, Guilin 541004, People's Republic of China

- ¹² Guangxi University, Nanning 530004, People's Republic of China
- ¹³ Hangzhou Normal University, Hangzhou 310036, People's Republic of China
- ¹⁴ Helmholtz Institute Mainz, Johann-Joachim-Becher-Weg 45, D-55099 Mainz, Germany
- ¹⁵ Henan Normal University, Xinxiang 453007, People's Republic of China
- ¹⁶ Henan University of Science and Technology, Luoyang 471003, People's Republic of China
- ¹⁷ Huangshan College, Huangshan 245000, People's Republic of China
- ¹⁸ Hunan University, Changsha 410082, People's Republic of China
- ¹⁹ Indiana University, Bloomington, Indiana 47405, USA
- ²⁰ (A)INFN Laboratori Nazionali di Frascati, I-00044, Frascati, Italy; (B)INFN and University of Perugia, I-06100, Perugia, Italy
- ²¹ (A)INFN Sezione di Ferrara, I-44122, Ferrara, Italy; (B)University of Ferrara, I-44122, Ferrara, Italy
- ²² Johannes Gutenberg University of Mainz, Johann-Joachim-Becher-Weg 45, D-55099 Mainz, Germany
- ²³ Joint Institute for Nuclear Research, 141980 Dubna, Moscow region, Russia
- ²⁴ Justus-Liebig-Universität Giessen, II. Physikalisches Institut, Heinrich-Buff-Ring 16, D-35392 Giessen, Germany
- ²⁵ KVI-CART, University of Groningen, NL-9747 AA Groningen, The Netherlands
- ²⁶ Lanzhou University, Lanzhou 730000, People's Republic of China
- ²⁷ Liaoning University, Shenyang 110036, People's Republic of China
- ²⁸ Nanjing Normal University, Nanjing 210023, People's Republic of China
- ²⁹ Nanjing University, Nanjing 210093, People's Republic of China
- ³⁰ Nankai University, Tianjin 300071, People's Republic of China
- ³¹ Peking University, Beijing 100871, People's Republic of China
- ³² Seoul National University, Seoul, 151-747 Korea
- ³³ Shandong University, Jinan 250100, People's Republic of China
- ³⁴ Shanghai Jiao Tong University, Shanghai 200240, People's Republic of China
- ³⁵ Shanxi University, Taiyuan 030006, People's Republic of China
- ³⁶ Sichuan University, Chengdu 610064, People's Republic of China
- ³⁷ Soochow University, Suzhou 215006, People's Republic of China
- ³⁸ Sun Yat-Sen University, Guangzhou 510275, People's Republic of China
- ³⁹ Tsinghua University, Beijing 100084, People's Republic of China
- ⁴⁰ (A)Ankara University, 06100 Tandogan, Ankara, Turkey; (B)Istanbul Bilgi University, 34060 Eyup, Istanbul, Turkey; (C)Uludag University, 16059 Bursa, Turkey; (D)Near East University, Nicosia, North Cyprus, Mersin 10, Turkey
- ⁴¹ University of Chinese Academy of Sciences, Beijing 100049, People's Republic of China
- ⁴² University of Hawaii, Honolulu, Hawaii 96822, USA
- ⁴³ University of Minnesota, Minneapolis, Minnesota 55455, USA
- ⁴⁴ University of Rochester, Rochester, New York 14627, USA
- ⁴⁵ University of Science and Technology Liaoning, Anshan 114051, People's Republic of China
- ⁴⁶ University of Science and Technology of China, Hefei 230026, People's Republic of China
- ⁴⁷ University of South China, Hengyang 421001, People's Republic of China
- ⁴⁸ University of the Punjab, Lahore-54590, Pakistan
- ⁴⁹ (A)University of Turin, I-10125, Turin, Italy; (B)University of Eastern Piedmont, I-15121, Alessandria, Italy; (C)INFN, I-10125, Turin, Italy
- ⁵⁰ Uppsala University, Box 516, SE-75120 Uppsala, Sweden
- ⁵¹ Wuhan University, Wuhan 430072, People's Republic of China
- ⁵² Zhejiang University, Hangzhou 310027, People's Republic of China
- ⁵³ Zhengzhou University, Zhengzhou 450001, People's Republic of China
- ^a Also at State Key Laboratory of Particle Detection and Electronics, Beijing 100049, Hefei 230026, People's Republic of China
- ^b Also at Bogazici University, 34342 Istanbul, Turkey
- ^c Also at the Moscow Institute of Physics and Technology, Moscow 141700, Russia
- ^d Also at the Functional Electronics Laboratory, Tomsk State University, Tomsk, 634050, Russia
- ^e Also at the Novosibirsk State University, Novosibirsk, 630090, Russia
- ^f Also at the NRC "Kurchatov Institute", PNPI, 188300, Gatchina, Russia
- ^g Also at University of Texas at Dallas, Richardson, Texas 75083, USA
- ^h Also at Istanbul Arel University, 34295 Istanbul, Turkey
- ⁱ Also at Goethe University Frankfurt, 60323 Frankfurt am Main, Germany
- ^j Also at Institute of Nuclear and Particle Physics, Shanghai Key Laboratory for Particle Physics and Cosmology, Shanghai 200240, People's Republic of China

Using 482 pb⁻¹ of e⁺e⁻ collision data collected at a center-of-mass energy of $\sqrt{s} = 4.009$ GeV with the BESIII detector, we measure the branching fractions of the decays $D_s^+ \rightarrow \mu^+ \nu_\mu$ and $D_s^+ \rightarrow \tau^+ \nu_\tau$. By constraining the ratio of decay rates of D_s^+ to $\tau^+ \nu_\tau$ and to $\mu^+ \nu_\mu$ to the Standard Model prediction, the branching fractions are determined to be $\mathcal{B}(D_s^+ \rightarrow \mu^+ \nu_\mu) = (0.495 \pm 0.067 \pm 0.026)\%$ and $\mathcal{B}(D_s^+ \rightarrow \tau^+ \nu_\tau) = (4.83 \pm 0.65 \pm 0.26)\%$. Using these branching fractions, we obtain a value

for the decay constant $f_{D_s^+}$ of $(241.0 \pm 16.3 \pm 6.5)$ MeV, where the first error is statistical and the second systematic.

PACS numbers: 13.20.Fc, 12.38.Qk, 14.40.Lb

I. INTRODUCTION

The simplest and cleanest decay modes of the D_s^+ meson, both theoretically and experimentally, are the purely leptonic decays. In the Standard Model (SM), D_s^+ leptonic decays proceed via the annihilation of the c and anti- s quarks into a virtual W^+ boson (Fig. 1). The decay rate is predicted [1] to be

$$\Gamma(D_s^+ \rightarrow \ell^+ \nu_\ell) = \frac{G_F^2}{8\pi} f_{D_s^+}^2 m_\ell^2 m_{D_s^+} \left(1 - \frac{m_\ell^2}{m_{D_s^+}^2}\right)^2 |V_{cs}|^2, \quad (1)$$

where $m_{D_s^+}$ is the D_s^+ mass, m_ℓ is the lepton mass, G_F is the Fermi coupling constant, $|V_{cs}|$ is the Cabibbo-Kobayashi-Maskawa matrix [2] element which takes the value equal to $|V_{ud}|$ of $0.97425(22)$ [3], and $f_{D_s^+}$ is the decay constant that is related to the wave-function overlap of the quark and antiquark. The D_s^+ meson leptonic decay is a process in which a spin-0 meson decays to a left-handed neutrino or a right-handed antineutrino. According to angular momentum conservation, the lepton ℓ^+ (ℓ^-) must be left-handed (right-handed). As a consequence, the leptonic decay of D_s^+ meson is helicity suppressed, which follows from the m_ℓ^2 dependence of the decay width. Taking the phase-space factor $(1 - m_\ell^2/m_{D_s^+}^2)^2$ into account, the leptonic branching fractions are in the ratio $e^+\nu_e : \mu^+\nu_\mu : \tau^+\nu_\tau \simeq 2 \times 10^{-5} : 1 : 10$. The decays to $\mu^+\nu_\mu$ and $\tau^+\nu_\tau$ can be measured experimentally, while $e^+\nu_e$ is beyond the sensitivity of the BESIII experiment.

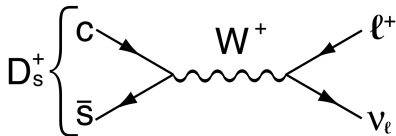


FIG. 1. Annihilation process for D_s^+ leptonic decays in the Standard Model.

Recently, the CLEO [4], *BABAR* [5], and Belle [6] collaborations have published updated measurements of the branching fractions of D_s^+ leptonic decays and the decay constant $f_{D_s^+}$, resulting in the new world average $f_{D_s^+} = (257.5 \pm 4.6)$ MeV [7]. Theoretical predictions of $f_{D_s^+}$ [8–13] are lower than this value. The most precise predictions are from lattice QCD; the combined $(2+1)$ - and $(2+1+1)$ -flavor result is (249.0 ± 1.2) MeV. There is an approximately two standard-deviation difference between the experimental average and the lattice QCD calculations. Several models of physics beyond the SM, such as the two-Higgs-doublet model [14] and the R -parity-violating model [15], may help to understand this differ-

ence. It is important to further investigate this difference both theoretically and experimentally.

In this paper, we report new measurements of the branching fractions of $D_s^+ \rightarrow \mu^+\nu_\mu$ and $D_s^+ \rightarrow \tau^+\nu_\tau$ (where we use the decay $\tau^+ \rightarrow \pi^+\bar{\nu}_\tau$) and use them to determine the decay constant $f_{D_s^+}$. We use 482 pb^{-1} [16] of e^+e^- annihilation data taken at 4.009 GeV with the BESIII detector. At this energy, D_s mesons are only produced in $D_s^+D_s^-$ pairs and the cross section of $D_s^+D_s^-$ is nearly maximal [17]. As other processes, such as $D_sD_s^*$ and $D_s^*D_s^*$, are not allowed kinematically, we benefit from the exceptional purity of the D_s^+ sample. Using the technique first introduced by the MARK III Collaboration [18, 19], we select single-tag events, where either D_s^+ or D_s^- is reconstructed, and then reconstruct the leptonic signal on the recoil side (signal side). In this paper, we choose nine hadronic modes with large branching fractions to reconstruct single-tag events: (a) $K_S^0 K^-$, (b) $K^+ K^- \pi^-$, (c) $K^+ K^- \pi^- \pi^0$, (d) $K_S^0 K^+ \pi^- \pi^-$, (e) $\pi^+ \pi^- \pi^-$, (f) $\pi^- \eta$ ($\eta \rightarrow \gamma\gamma$), (g) $\pi^- \pi^0 \eta$ ($\eta \rightarrow \gamma\gamma$), (h) $\pi^- \eta'$ ($\eta' \rightarrow \pi^+ \pi^- \eta, \eta \rightarrow \gamma\gamma$), and (i) $\pi^- \eta'(\eta' \rightarrow \pi^+ \pi^- \gamma)$. For convenience, we denote the single tag as D_s^- and the leptonic decays as D_s^+ , although charge-conjugate states are also included.

II. DETECTOR AND MONTE CARLO

The BESIII detector [20] is designed to study hadron spectroscopy and τ -charm physics [21]. The cylindrical BESIII is composed of a helium-gas based drift chamber (MDC), a time-of-flight (TOF) system, a CsI(Tl) electromagnetic calorimeter (EMC), and a RPC-based muon chamber (MUC), with a superconducting magnet providing a 1.0 T magnetic field in the central region of the detector. The MDC covers the polar angle range $|\cos\theta| < 0.93$, with a momentum resolution of 0.5% for charged particles at 1 GeV/c and 6% resolution in the specific energy loss dE/dx . The TOF subdetector consists of two parts, the barrel and end cap. The intrinsic time resolution for the barrel counters is 80 ps, while for the end-cap counters it is 110 ps. The EMC measures energies and positions of electrons and photons with an energy resolution of 2.5% (5%) at an energy of 1 GeV in the barrel (end cap) region. The MUC is designed to have the ability to identify more than 90% of muons with momentum over 0.5 GeV, while misidentifying less than 10% of charged pions as muons.

We generate two Monte Carlo (MC) simulated samples for background analysis and efficiency measurement. The first sample is a generic MC sample, which corresponds to an equivalent integrated luminosity of about

20 times the data luminosity and includes open charm processes, continuum production of hadrons, QED processes and initial-state radiation (ISR) processes. The open-charm processes are simulated at the center-of-mass energy of 4.009 GeV, and their cross sections are taken from Ref. [17]. The second sample is an exclusive signal MC sample, in which the D_s^- meson decays to one of the single-tag modes while the D_s^+ meson decays to $\mu^+\nu_\mu$ or $\tau^+\nu_\tau$ ($\tau^+ \rightarrow \pi^+\bar{\nu}_\tau$). The simulation, including the beam-energy spread, ISR [22] and final-state radiation [23], is implemented with KKMC [24]. The known decay modes are generated with EVTGEN [25] with branching fractions set to the world average values [7], while the unmeasured decays are generated with LUNDCHARM [26].

III. SELECTION OF D_s^- SINGLE TAG

At $\sqrt{s} = 4.009$ GeV, D_s can only be produced in $D_s^+D_s^-$ pairs. If therefore a D_s^- meson is tagged, the recoil side is guaranteed to be a D_s^+ . The D_s^- tag is reconstructed from combinations of charged particles and photons in the event. For charged particles, the polar angles must satisfy $|\cos\theta| < 0.93$, and the points of closest approach to the e^+e^- interaction point (IP) must be within ± 10 cm along the beam direction and within 1 cm in the plane perpendicular to the beam direction. Charged pions and kaons must satisfy particle identification (PID) requirements. We calculate the confidence levels for the pion (kaon) ($CL_{\pi(K)}$) hypothesis by combining the ionization energy loss (dE/dx) in the MDC and the flight time obtained from the TOF. The pion (kaon) candidates are required to satisfy $CL_{\pi(K)} > CL_{K(\pi)}$.

For photon candidates, we require that the deposited energy of a neutral shower in the EMC is larger than 25 MeV in the barrel region ($|\cos\theta| < 0.8$) or larger than 50 MeV in the end-cap region ($0.86 < |\cos\theta| < 0.92$). To suppress electronic noise and energy deposits unrelated to the event, the EMC timing of the cluster (T) with respect to the event start time is required to satisfy $0 \leq T \leq 700$ ns. Photon candidates must be separated by at least 10 degrees from the extrapolated position of any charged track in the EMC.

The π^0 and η mesons are reconstructed in their $\gamma\gamma$ decay modes. We reject a combination if both photons are detected in the end-cap of the EMC. The invariant mass of the two photons $M(\gamma\gamma)$ is required to be within $0.115 < M(\gamma\gamma) < 0.150$ GeV/ c^2 for π^0 and $0.51 < M(\gamma\gamma) < 0.57$ GeV/ c^2 for η , respectively. To improve the resolution, the $\gamma\gamma$ invariant mass is constrained to the nominal π^0 or η mass [7], and the resultant momenta are used in the subsequent analysis. The η' meson is reconstructed in the $\pi^+\pi^-\eta$ and $\pi^+\pi^-\gamma$ final states. The invariant masses are required to satisfy $0.943 < M(\pi^+\pi^-\gamma\gamma) < 0.973$ GeV/ c^2 and $0.932 < M(\pi^+\pi^-\gamma) < 0.980$ GeV/ c^2 for these two modes, respectively.

Candidates for K_S^0 are reconstructed from pairs of oppositely charged tracks without requirements on PID and their distances to the IP. The secondary vertex is required to be separated from the IP by a decay length of at least twice the vertex resolution. The invariant mass of the track pair (assuming both tracks are pions) $M(\pi^+\pi^-)$ is required to be within $0.487 < M(\pi^+\pi^-) < 0.511$ GeV/ c^2 .

Two kinematic variables (ΔE , M_{BC}) reflecting energy and momentum conservation are used to identify D_s^- candidates. First, we calculate the energy difference

$$\Delta E = E_{D_s^-} - E_{\text{beam}}, \quad (2)$$

where $E_{D_s^-}$ is the reconstructed energy of a D_s^- meson and E_{beam} is the beam energy. Correctly reconstructed signal events peak around zero in the ΔE distribution. The ΔE requirements listed in Table I cover about 95% of the signal events. We keep the combination with the smallest $|\Delta E|$ for each D_s^- tag mode. The second variable is the beam-energy-constrained mass

$$M_{BC} = \sqrt{E_{\text{beam}}^2/c^4 - \vec{p}_{D_s^-}^2/c^2}, \quad (3)$$

where $\vec{p}_{D_s^-}$ is the total momentum of the particles that form the D_s^- candidate. Figure 2 shows the M_{BC} distributions for data. We determine the single-tag yields by fitting the M_{BC} distributions. In the fits, we use the MC-determined signal shapes convolved with a Gaussian function with free mean and resolution to model the signal and an ARGUS [27] function for the background. We accept the events satisfying $1.962 < M_{BC} < 1.982$ GeV/ c^2 for further analysis. This range contains about 95% of the signal events. Table I lists the single-tag yields by tag mode, with an overall total of 15127 ± 321 D_s^- events.

IV. ANALYSIS OF D_s^+ LEPTONIC SIGNAL

A. Selection of D_s^+ leptonic signal

In events containing a selected tag candidate, we search for the D_s^+ leptonic decays to $\mu^+\nu_\mu$ and $\tau^+\nu_\tau$ ($\tau^+ \rightarrow \pi^+\bar{\nu}_\tau$) by using the other final-state particles that are not used to reconstruct the D_s^- tag. We require that there is exactly one good charged track in the signal side, and that the charge of the track is opposite to the D_s^- tag. The track satisfies the selection criteria (without PID requirements) for charged tracks given in Sec. III. We also require the energy of the most energetic neutral cluster in the EMC not associated with the tag D_s^- to be less than 300 MeV to eliminate background events that contain photon(s). If there are multiple D_s^+ candidates in an event, we only keep the one with the D_s^- tag with the smallest $|\Delta E|$ for further analysis.

To characterize the signal events of $D_s^+ \rightarrow \ell^+\nu_\ell$, the

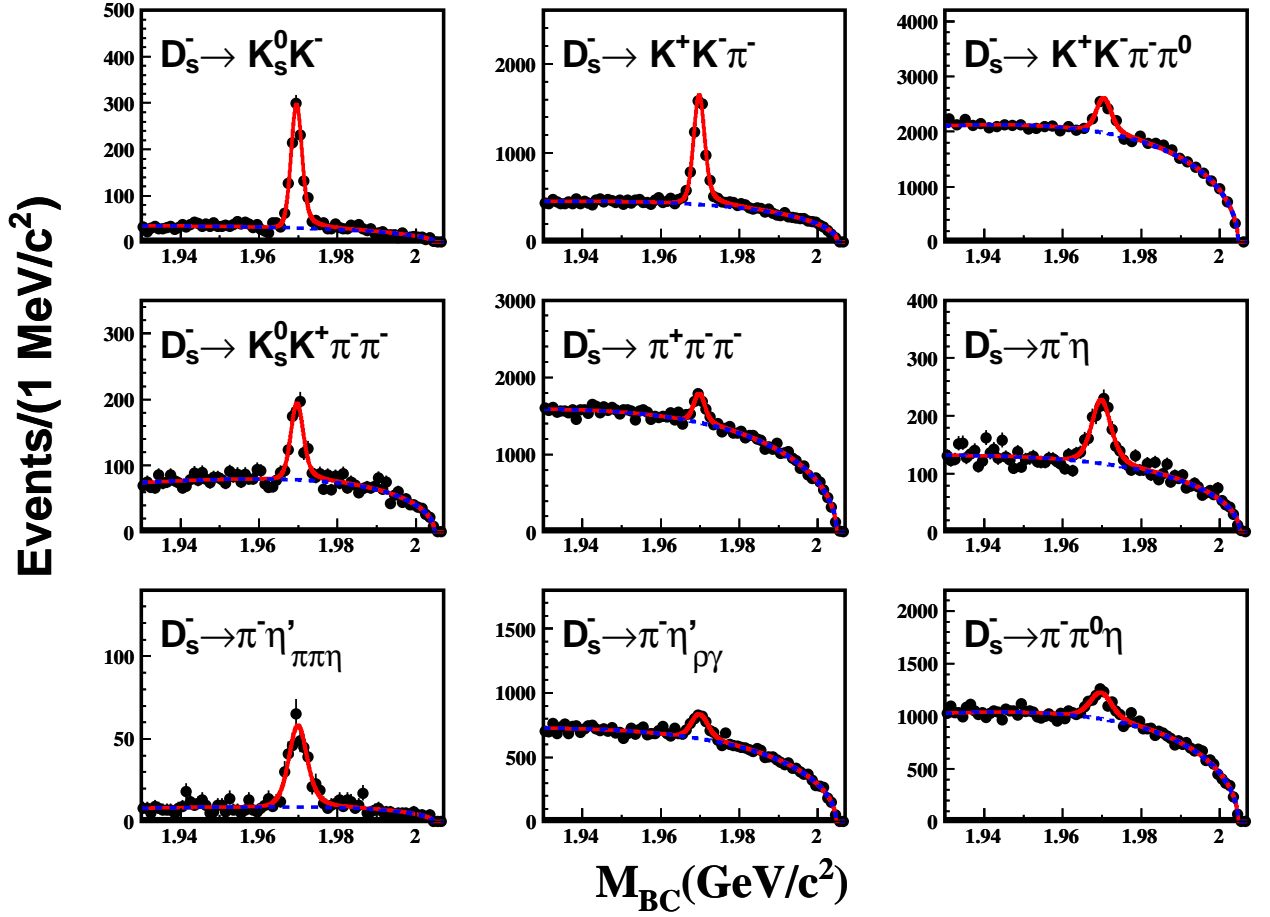


FIG. 2. Fits to the M_{BC} distributions of D_s^- candidates. The points with error bars are data. The red curves are the fit results. The blue dashed curves are the fitted combinatorial backgrounds.

TABLE I. Requirements on ΔE and M_{BC} , detection efficiencies and event yields for the different single-tag modes from data (the errors are statistical).

Mode	ΔE (MeV)	M_{BC} (MeV)	ϵ_{tag} (%)	$\epsilon_{\text{tag}, \mu\nu}$ (%)	$\epsilon_{\text{tag}, \tau\nu}$ (%)	N_{tag}
$K_s^0 K^-$	(-27, 21)	(1962, 1982)	46.76 ± 0.34	43.97 ± 0.22	20.14 ± 0.18	1065 ± 39
$K^+ K^- \pi^-$	(-32, 23)		42.45 ± 0.18	37.17 ± 0.22	17.55 ± 0.17	5172 ± 114
$K^+ K^- \pi^- \pi^0$	(-41, 22)		12.71 ± 0.21	12.97 ± 0.15	6.11 ± 0.11	1900 ± 140
$K_s^0 K^+ \pi^- \pi^-$	(-35, 24)		23.37 ± 0.36	24.21 ± 0.19	11.50 ± 0.14	576 ± 48
$\pi^+ \pi^- \pi^-$	(-36, 23)		58.27 ± 0.87	49.45 ± 0.22	23.06 ± 0.19	1606 ± 139
$\pi^- \eta$	(-38, 37)		46.34 ± 0.67	42.30 ± 0.25	19.66 ± 0.18	814 ± 52
$\pi^- \pi^0 \eta$	(-35, 27)		24.69 ± 0.31	24.27 ± 0.14	11.18 ± 0.10	2172 ± 150
$\pi^- \eta' (\eta' \rightarrow \pi^+ \pi^- \eta)$	(-35, 22)		27.83 ± 0.49	24.43 ± 0.19	11.59 ± 0.14	440 ± 39
$\pi^- \eta' (\eta' \rightarrow \pi^+ \pi^- \gamma)$	(-53, 30)		41.83 ± 0.86	34.54 ± 0.21	16.28 ± 0.17	1383 ± 143

missing mass squared (MM^2) is defined as

$$MM^2 = (E_{\text{beam}} - E_{\mu^+})^2 / c^4 - \left(-\vec{p}_{D_s^-} - \vec{p}_{\mu^+} \right)^2 / c^2, \quad (4)$$

where E_{μ^+} and \vec{p}_{μ^+} are the energy and momentum of the muon candidate. For $D_s^+ \rightarrow \mu^+ \nu_\mu$ events, the MM^2 should peak around zero since there is only one miss-

ing neutrino. For $D_s^+ \rightarrow \tau^+ \nu_\tau (\tau^+ \rightarrow \pi^+ \bar{\nu}_\tau)$ events, the MM^2 (assuming the track is a muon when calculating the MM^2) has a broad structure due to the presence of the two neutrinos. In this study, the signal region considered is $-0.15 < MM^2 < 0.20$ (GeV/c^2)², where the higher limit is imposed to exclude background events [e.g. $\eta\pi^+$, $K^0\pi^+$, $\tau^+\nu_\tau (\tau^+ \rightarrow \pi^+\pi^0\bar{\nu}_\tau)$, etc.] that contribute significantly above 0.20 (GeV/c^2)².

B. Background estimation

Two classes of background events are considered in this analysis. The first one contains D_s^+ events in which the single-tag D_s^- is correctly reconstructed but the signal side is misreconstructed ($\tau^+ \rightarrow \mu^+ \nu_\mu \bar{\nu}_\mu$, $\tau^+ \rightarrow \pi^+ \pi^0 \bar{\nu}_\mu$ and many other D_s^+ decays are considered). The second class contains the non- D_s^+ background, which is expected to be a smooth distribution under the D_s^- peak in the M_{BC} spectra. We investigate the real D_s^+ background by examining the $D_s^+ D_s^-$ events in the generic MC sample with the signal events excluded. After all selection criteria are imposed, a total of 104 events survive, which is equivalent to 7.0 ± 0.7 events for the 482 pb^{-1} of data. For the analysis, we fix the shape and size of this background in the MM^2 fits. We estimate the contribution of the second class of background using candidate events in the M_{BC} sideband, which is defined as $(1.946, 1.956) \text{ GeV}/c^2$ and $(1.986, 2.000) \text{ GeV}/c^2$. The background integral in the sideband region is the same as in the signal region.

C. D_s^+ detection efficiencies

The overall detection efficiency for $D_s^+ \rightarrow \ell^+ \nu_\ell$ can be expressed as

$$\epsilon = \sum_i \left(\frac{N_{\text{tag}}^i}{N_{\text{tag}}} \times \frac{\epsilon_{\text{tag,sig}}^i}{\epsilon_{\text{tag}}^i} \right), \quad (5)$$

where N_{tag}^i is the number of events for single-tag mode i , N_{tag} is the number of events for all single-tag modes, $\epsilon_{\text{tag,sig}}^i$ is the efficiency of detecting both the single-tag mode i and the leptonic decays, and ϵ_{tag}^i is the efficiency of detecting the single-tag mode i . We determine $\epsilon_{\text{tag,sig}}^i$ by analyzing the signal MC sample and ϵ_{tag}^i by analyzing the generic MC sample (Table I). The overall signal efficiencies are measured to be $(91.4 \pm 0.5)\%$ and $(41.0 \pm 0.3)\%$ for $D_s^+ \rightarrow \mu^+ \nu_\mu$ and $D_s^+ \rightarrow \tau^+ \nu_\tau$ ($\tau^+ \rightarrow \pi^+ \bar{\nu}_\tau$), respectively, where the errors are from MC statistics. It is worth noting that the large efficiency difference between these two signal channels is mainly caused by the upper limit on MM^2 .

D. Branching fractions

The branching fraction of the D_s^+ leptonic decay is calculated by

$$\mathcal{B}(D_s^+ \rightarrow \ell^+ \nu_\ell) = \frac{N_{\text{sig}}}{N_{\text{tag}} \times \epsilon}, \quad (6)$$

where N_{sig} is the number of the signal events that is determined by a fit to the MM^2 spectra. In this work, we fit the MM^2 spectra in two different ways, as described in the following sections.

1. The SM-constrained fit

For the finally selected candidates, we fit the MM^2 spectra by constraining the ratio of $\mu^+ \nu_\mu$ and $\tau^+ \nu_\tau$ decay rates to the SM prediction,

$$R \equiv \frac{\Gamma(D_s^+ \rightarrow \tau^+ \nu_\tau)}{\Gamma(D_s^+ \rightarrow \mu^+ \nu_\mu)} = \frac{m_{\tau^+}^2 \left(1 - \frac{m_{\tau^+}^2}{m_{D_s^+}^2}\right)^2}{m_{\mu^+}^2 \left(1 - \frac{m_{\mu^+}^2}{m_{D_s^+}^2}\right)^2} = 9.76. \quad (7)$$

An unbinned extended maximum likelihood fit to the events in the M_{BC} signal region and those in the M_{BC} sideband is performed simultaneously, as shown in Fig. 3. In this fit, the ratio of the number of the $\mu^+ \nu_\mu$ and $\tau^+ \nu_\tau$ signal events is constrained according to the SM prediction on R , the overall signal efficiencies (mentioned in Sec. IV C) and the branching fraction of $\tau^+ \rightarrow \pi^+ \bar{\nu}_\tau$. The shapes of the $\mu^+ \nu_\mu$ and $\tau^+ \nu_\tau$ signals are determined by the MC shapes convolved with a Gaussian function, the shape and yield of the real D_s^+ background are fixed by the MC estimation, and the non- D_s^+ background is modeled by a first-order polynomial function with parameters and size constrained by the events in the D_s^- sideband in the simultaneous fit. We obtain yields of 69.3 ± 9.3 $D_s^+ \rightarrow \mu^+ \nu_\mu$ events and 32.5 ± 4.3 $D_s^+ \rightarrow \tau^+ \nu_\tau$ ($\tau^+ \rightarrow \pi^+ \bar{\nu}_\tau$) events, respectively. Following Dobrescu and Kronfeld's calculation [28, 29], we lower the measured $\mathcal{B}(D_s^+ \rightarrow \mu^+ \nu_\mu)$ by 1% to account for the contribution of the $\gamma \mu^+ \nu_\mu$ final state. The corrected branching fraction is

$$\mathcal{B}(D_s^+ \rightarrow \mu^+ \nu_\mu) = (0.495 \pm 0.067)\%, \quad (8)$$

where the error includes the statistical uncertainties of the single-tag yields and of the signal yield. The corresponding branching fraction of $D_s^+ \rightarrow \tau^+ \nu_\tau$ is obtained to be

$$\mathcal{B}(D_s^+ \rightarrow \tau^+ \nu_\tau) = (4.83 \pm 0.65)\%. \quad (9)$$

2. The non-SM-constrained fit

Alternatively, we perform a fit to the MM^2 spectra leaving the ratio of $\mu^+ \nu_\mu$ and $\tau^+ \nu_\tau$ events to be free, so that we can measure the branching fractions of $D_s^+ \rightarrow \mu^+ \nu_\mu$ and $D_s^+ \rightarrow \tau^+ \nu_\tau$ independently. As shown in Fig. 3, it is difficult to distinguish the $\tau^+ \nu_\tau$ signal and background in the high MM^2 region. We attempt to improve this situation by taking advantage of the EMC and MUC information.

We use two criteria that help to discriminate muons from pions. In principle, muons can penetrate in the MUC detector much deeper than hadrons. Therefore, the penetration depth in the MUC can provide strong discrimination power for muons and pions. To select a

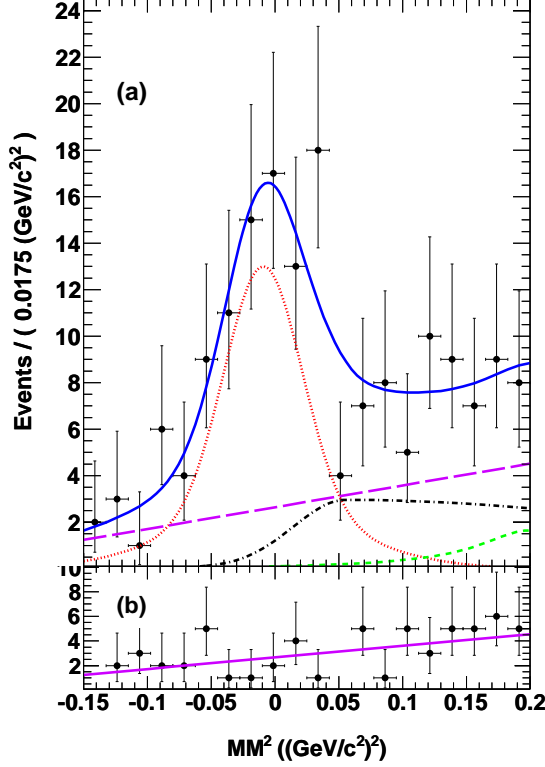


FIG. 3. Projections of the simultaneous fit to the MM^2 distributions of the events in (a) the D_s^- signal region and (b) M_{BC} sideband region. Data are shown as the points with error bars. The red dotted curve shows the $\mu^+\nu_\mu$ signal and the black dot-dashed curve shows the $\tau^+\nu_\tau$ signal. The purple long-dashed line shows the non- D_s^+ background while the green dashed line shows the real- D_s^+ background. The blue curve shows the sum of all these contributions.

muon-enriched sample, we impose the following condition (μ - id) on the MUC depth d : for $p < 1.1$ GeV/ c , we require $d > (75 pc/\text{GeV} - 40.5)$ cm, while for $p > 1.1$ GeV/ c , we require $d > 42$ cm, where p denotes the momentum of the charged track. This requirement achieves good separation of muons from pions.

The charged tracks deposit energy in the EMC by ionization. For pions, the deposited energies tend to have larger values due to nuclear interactions in the EMC materials. The condition (π - id) to select a pion-enriched sample is $E_{\text{EMC}} > 0.3$ GeV.

We use the above two conditions to separate the $\ell^+\nu_\ell$ candidates into three subsamples. Subsample I contains events that pass the μ - id but fail the π - id . Subsample II consists of events that fail both μ - id and π - id . Subsample III consists of events that pass the π - id . As a result, subsamples I and III are dominated by muons and pions, respectively, while subsample II has comparable numbers of muons and pions. We measure the relative fractions of muon (pion) ($\epsilon_{\mu(\pi),\text{data}}$) in the three subsamples using

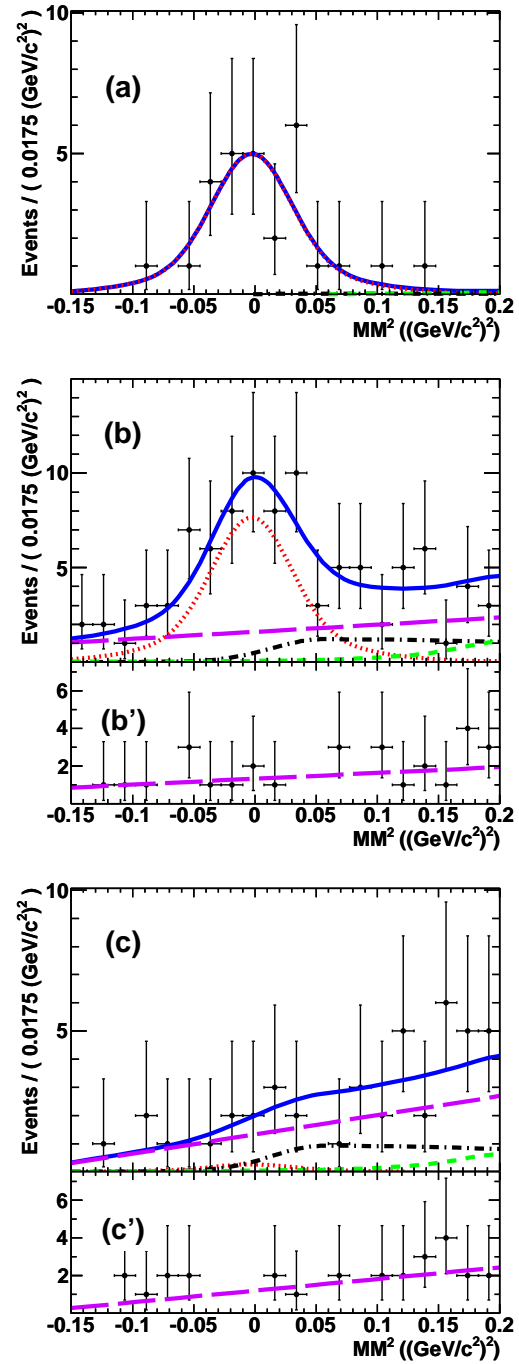


FIG. 4. Projections of the simultaneous fit to the MM^2 distributions of (a) part I, (b) part II and (c) part III data subsamples as defined in Sec. IV D 2. (b') and (c') are the corresponding MM^2 distributions from the M_{BC} sideband. Data are shown as the points with error bars. The red dotted curve shows the $\mu^+\nu_\mu$ signal and the black dot-dashed curve shows the $\tau^+\nu_\tau$ signal. The purple long-dashed line shows the non- D_s^+ background while the green dashed line shows the real- D_s^+ background. The blue curve shows the sum of all these contributions.

$e^+e^- \rightarrow \mu^+\mu^- [\psi(2S) \rightarrow \pi^+\pi^- J/\psi (J/\psi \rightarrow \rho\pi)]$ events in data. Then we perform a two-dimensional correction (with respect to momentum and polar angle distributions of the muons or pions in signal MC) to $\epsilon_{\mu(\pi),\text{data}}$, and obtain the relative fractions of $\mu^+\nu_\mu$ ($\tau^+\nu_\tau$) ($\epsilon_{\mu\nu(\tau\nu),\text{data}}$) in the three subsamples. Table II lists the measured $\mu^+\nu_\mu$ and $\tau^+\nu_\tau$ relative fractions in the three subsamples in data.

TABLE II. Relative signal fractions (%) in the three subsamples (errors are statistical).

	I	II	III
$\mu^+\nu_\mu$	45.6 ± 0.5	52.9 ± 0.7	1.9 ± 0.4
$\tau^+\nu_\tau$	1.9 ± 0.1	54.8 ± 0.6	43.6 ± 0.6

We perform a simultaneous fit to the MM² spectra for the events in the three subsamples, constraining the ratio of $\mu^+\nu_\mu$ to be 45.6 : 52.9 : 1.9 and the ratio of $\tau^+\nu_\tau$ to be 1.9 : 54.8 : 43.6. From the fit, as shown in Fig. 4, we obtain $72.4 \pm 10.4 D_s^+ \rightarrow \mu^+\nu_\mu$ events and $22.1 \pm 12.3 D_s^+ \rightarrow \tau^+\nu_\tau$ ($\tau^+ \rightarrow \pi^+\bar{\nu}_\tau$) events. Applying the correction of 1%, we find the branching fractions to be

$$\mathcal{B}(D_s^+ \rightarrow \mu^+\nu_\mu) = (0.517 \pm 0.075)\%, \quad (10)$$

and

$$\mathcal{B}(D_s^+ \rightarrow \tau^+\nu_\tau) = (3.28 \pm 1.83)\%. \quad (11)$$

These results are consistent with those determined from the fit by constraining the $\tau^+\nu_\tau/\mu^+\nu_\mu$ ratio to the SM prediction. This method can be used to test lepton universality, which demands that the $\tau^+\nu_\tau/\mu^+\nu_\mu$ ratio only depend on the muon and tau masses. With the currently available data sample, this test is statistics-limited.

E. Systematic uncertainties

Table III summarizes the systematic uncertainties for the branching fraction measurements. The uncertainty due to the single-tag yield is estimated by varying the fit range and background shape. The uncertainty due to the efficiency of finding a muon or charged pion is taken to be 1% per track [30]. The uncertainty from the efficiency of the extra shower requirement is studied with the hadronic control samples $\psi(2S) \rightarrow \pi^+\pi^- J/\psi (J/\psi \rightarrow \mu^+\mu^-)$, $\psi(2S) \rightarrow 3(\pi^+\pi^-)$ and $\psi(2S) \rightarrow K^+K^- 2(\pi^+\pi^-)$. We fully reconstruct these three samples and measure the efficiencies for the extra shower requirement for data and MC, respectively. The efficiency difference is taken as the systematic uncertainty. Uncertainties related to the MM² fits include the MM² resolution, MM² fit range, background estimation and signal fractions in subsamples. The uncertainty from the MM² resolution is estimated by changing the resolution of the convolved Gaussian function in signal shape; the uncertainty from the

MM² fit range is estimated by shifting the range by ± 10 (MeV/c²)²; the uncertainty due to the background is estimated by varying the number of background events by $\pm 1\sigma$, assuming that the number of background events follow a Poisson distribution, for the real- D_s background, and varying the sideband range and background shape for the non- D_s background; the uncertainty from the relative signal fractions in the subsamples is estimated by varying the fractions by ± 1 statistical error. The systematic error associated with Dobrescu and Kronfeld's calculation [28] of the contribution of the $\gamma\mu^+\nu_\mu$ decay mode could be 1% of the lowest-order mechanism for photon momenta below 300 MeV. We take 100% of this correction value, which is 1%, as the systematic error. In addition to these, we have considered uncertainties arising from $\mathcal{B}(\tau^+ \rightarrow \pi^+\bar{\nu}_\tau)$ [7] and MC statistics of the detection efficiencies.

F. Decay constant $f_{D_s^+}$

The decay constant $f_{D_s^+}$ can be determined using Eq. (1). By substituting $\mathcal{B}(D_s^+ \rightarrow \ell^+\nu_\ell) = \tau_{D_s^+} \Gamma(D_s^+ \rightarrow \ell^+\nu_\ell)$, where $\tau_{D_s^+}$ is the D_s^+ lifetime, we obtain

$$f_{D_s^+} = \frac{1}{G_F m_\ell \left(1 - \frac{m_\ell^2}{m_{D_s^+}^2}\right) |V_{cs}|} \sqrt{\frac{8\pi \mathcal{B}(D_s^+ \rightarrow \ell^+\nu_\ell)}{m_{D_s^+} \tau_{D_s^+}}} \quad (12)$$

We use the $\mathcal{B}(D_s^+ \rightarrow \mu^+\nu_\mu)$ result of Eq. (8) to calculate the decay constant. Inserting G_F , m_μ , $m_{D_s^+}$, $|V_{cs}| = |V_{ud}| = 0.97425(22)$ [7], and the measured $\mathcal{B}(D_s^+ \rightarrow \mu^+\nu_\mu)$, we determine the decay constant to be

$$f_{D_s^+} = (241.0 \pm 16.3 \pm 6.6) \text{ MeV}, \quad (13)$$

where the first error is statistical and the second systematic. Systematic uncertainties include uncertainties in the measured branching fractions and the input parameters, and the latter one is dominated by the D_s^+ lifetime, which is 0.7%.

V. CONCLUSION

In this paper, we have measured the branching fractions of $D_s^+ \rightarrow \mu^+\nu_\mu$ and $D_s^+ \rightarrow \tau^+\nu_\tau$ using 482 pb⁻¹ of data taken at 4.009 GeV. Our results within the context of the SM are

$$\mathcal{B}(D_s^+ \rightarrow \mu^+\nu_\mu) = (0.495 \pm 0.067 \pm 0.026)\%, \quad (14)$$

and

$$\mathcal{B}(D_s^+ \rightarrow \tau^+\nu_\tau) = (4.83 \pm 0.65 \pm 0.26)\%. \quad (15)$$

Using these branching fractions, the decay constant $f_{D_s^+}$ is determined as shown in Eq. (13).

TABLE III. Systematic uncertainties (%) for the branching fraction measurements.

Sources	Constrained measurement		Unconstrained measurement	
	$D_s^+ \rightarrow \mu^+ \nu_\mu$	$D_s^+ \rightarrow \tau^+ \nu_\tau$	$D_s^+ \rightarrow \mu^+ \nu_\mu$	$D_s^+ \rightarrow \tau^+ \nu_\tau$
Number of tags	1.7	1.7	1.7	1.7
Track finding	1.0	1.0	1.0	1.0
Extra shower cut	0.5	0.5	0.5	0.5
MM ² resolution	2.3	2.3	2.5	5.5
MM ² fitting range	1.2	1.6	1.8	0.3
Background	4.4	4.4	2.3	9.4
Relative signal fractions in the three subsamples	-	-	1.1	1.1
Radiative correction	1.0	-	1.0	-
$\mathcal{B}(\tau^+ \rightarrow \pi^+ \bar{\nu}_\tau)$	-	0.6	-	0.6
MC statistics	0.5	0.6	0.5	0.6
Sum	5.6	5.7	4.6	11.2

We have also measured the branching fractions without constraining the $\tau^+ \nu_\tau$ and $\mu^+ \nu_\mu$ decay rates to the SM prediction, and the results are

$$\mathcal{B}(D_s^+ \rightarrow \mu^+ \nu_\mu) = (0.517 \pm 0.075 \pm 0.021)\%, \quad (16)$$

and

$$\mathcal{B}(D_s^+ \rightarrow \tau^+ \nu_\tau) = (3.28 \pm 1.83 \pm 0.37)\%. \quad (17)$$

The branching fraction for $D_s^+ \rightarrow \mu^+ \nu_\mu$ measured in this work is consistent with the experimental world average [7] within one standard deviation, while the branching fraction for $D_s^+ \rightarrow \tau^+ \nu_\tau$ is about 1.5 standard deviations lower. The measured decay constant $f_{D_s^+}$ is consistent with the average of the lattice QCD calculations [8–13]. With the pure $D_s^+ D_s^-$ sample, we provide an overall competitive result in spite of low statistics. As for the future, BESIII is taking data at $\sqrt{s} = 4.18$ GeV, in which $D_s D_s^*$ production is maximal, and we will be able to significantly improve the measurement of the decay constant $f_{D_s^+}$.

Acknowledgements

The BESIII Collaboration thanks the staff of BEPCII and the IHEP computing center for their strong support. This work is supported in part by National Key Basic Research Program of China under Contract

No. 2015CB856700, 2009CB825204; National Natural Science Foundation of China (NSFC) under Contracts Nos. 11125525, 11235011, 11322544, 11335008, 11425524, 11205163, 10935007; the Chinese Academy of Sciences (CAS) Large-Scale Scientific Facility Program; the CAS Center for Excellence in Particle Physics (CCEPP); the Collaborative Innovation Center for Particles and Interactions (CICPI); Joint Large-Scale Scientific Facility Funds of the NSFC and CAS under Contracts Nos. 11179007, U1232201, U1332201; CAS under Contracts Nos. KJCX2-YW-N29, KJCX2-YW-N45; 100 Talents Program of CAS; National 1000 Talents Program of China; INPAC and Shanghai Key Laboratory for Particle Physics and Cosmology; German Research Foundation DFG under Contracts Nos. Collaborative Research Center CRC 1044, FOR 2359; Istituto Nazionale di Fisica Nucleare, Italy; Koninklijke Nederlandse Akademie van Wetenschappen (KNAW) under Contract No. 530-4CDP03; Ministry of Development of Turkey under Contract No. DPT2006K-120470; National Natural Science Foundation of China (NSFC) under Contracts Nos. 11405046, U1332103; Russian Foundation for Basic Research under Contract No. 14-07-91152; The Swedish Research Council; U. S. Department of Energy under Contracts Nos. DE-FG02-05ER41374, DE-SC-0010504, de-sc0012069, DESC0010118; U.S. National Science Foundation; University of Groningen (RuG) and the Helmholtzzentrum fuer Schwerionenforschung GmbH (GSI), Darmstadt; WCU Program of National Research Foundation of Korea under Contract No. R32-2008-000-10155-0.

[1] D. Silverman and H. Yao, Phys. Rev. D **38**, 214 (1988).
[2] M. Kobayashi and T. Maskawa, Prog. Theor. Phys. **49**, 652 (1973)
[3] J.C. Hardy and I.S. Towner, Phys. Rev. C **79**, 055502 (2009).
[4] J.P. Alexander *et al.* [CLEO Collaboration], Phys. Rev. D **79**, 052001 (2009).
[5] P. del Amo Sanchez *et al.* [BABAR Collaboration], Phys.

Rev. D **82**, 091103(R) (2010).
[6] A. Zupanc *et al.* [Belle Collaboration], JHEP **09**, 139 (2013).
[7] K.A. Olive *et al.* [Particle Data Group], Chin. Phys. C **38**, 090001 (2014).
[8] N. Carrasco, P. Dimopoulos, R. Frezzotti, P. Lami, V. Lubicz, F. Nazzaro, E. Picca, L. Riggio, G.C. Rossi, F. Sanfilippo, S. Simula, C. Tarantino, Phys. Rev. D **91**,

- 054507 (2015).
- [9] A. Bazavov *et al.*, Phys. Rev. D **90**, 074509 (2014).
 - [10] Y.B. Yang, Y. Chen, A. Alexandru, S.J. Dong, T. Draper, M. Gong, F.X. Lee, A. Li, K.F. Liu, Z. Liu, M. Lujan, Phys. Rev. D **92**, 034517 (2015).
 - [11] H. Na, C.T.H. Davies, E. Follana, G.P. Lepage and J. Shigemitsu, Phys. Rev. D **86**, 054510 (2012).
 - [12] A. Bazavov *et al.*, Phys. Rev. D **85**, 114506 (2012).
 - [13] C.T.H. Davies, C. McNeile, E. Follana, G.P. Lepage, H. Na and J. Shigemitsu, Phys. Rev. D **82**, 114504 (2010).
 - [14] A.G. Akeroyd and C.H. Chen, Phys. Rev. D **75**, 075004 (2007).
 - [15] A.G. Akeroyd and S. Recksiegel, Phys. Lett. B **554**, 38 (2003).
 - [16] M. Ablikim *et al.* [BESIII Collaboration], Chin. Phys. C **39**(9), 093001 (2015).
 - [17] D. Cronin-Hennessy *et al.* [CLEO Collaboration], Phys. Rev. D **80**, 072001 (2009).
 - [18] R.M. Baltrusaitis *et al.* [MARK-III Collaboration], Phys. Rev. Lett. **56**, 2140 (1986).
 - [19] J. Adler *et al.* [MARK-III Collaboration], Phys. Rev. Lett. **60**, 89 (1988).
 - [20] M. Ablikim *et al.* [BESIII Collaboration], Nucl. Instrum. Meth. A **614**, 345 (2010).
 - [21] D.M. Asner *et al.*, Int. J. Mod. Phys. A **24**, 499 (2009).
 - [22] E.A. Kureav and V.S. Fadin, Sov. J. Nucl. Phys. **41**, 466 (1985).
 - [23] E. Richter-Was, Phys. Lett. B **303**, 163 (1993).
 - [24] S. Jadach, B.F.L. Ward and Z. Was, Phys. Rev. D **63**, 113009 (2001).
 - [25] D.J. Lange, Nucl. Instrum. Meth. A **462**, 152 (2001); R.G. Ping, Chin. Phys. C **320**, 599 (2008).
 - [26] J.C. Chen, G.S. Huang, X.R. Qi, D.H. Zhang and Y.S. Zhu, Phys. Rev. D **62**, 034003 (2000).
 - [27] H. Albrecht *et al.* [ARGUS Collaboration], Phys. Lett. B **229**, 304 (1989).
 - [28] B.A. Dobrescu and A.S. Kronfeld, Phys. Rev. Lett. **100**, 241802 (2008).
 - [29] G. Burdman, T. Goldman, and D. Wyler, Phys. Rev. D **51**, 111 (1995).
 - [30] M. Ablikim *et al.* [BESIII Collaboration], Phys. Rev. D **86**, 071101 (2012).